

PRINTER: Deformation-Aware Adversarial Learning for Virtual IHC Staining with In Situ Fidelity

Yizhe Yuan*
Shanghai Jiao Tong University
Shanghai, China
yuanyz0825@sjtu.edu.cn

Bingsen Xue*
Shanghai Jiao Tong University
Shanghai, China
bingsenxue@sjtu.edu.cn

Bangzheng Pu
Shanghai Jiao Tong University
Shanghai, China
bangzheng@sjtu.edu.cn

Chengxiang Wang
Shanghai Jiao Tong University
Shanghai, China
wcx123@sjtu.edu.cn

Cheng Jin†
Shanghai Jiao Tong University
Shanghai, China
chengjin520@sjtu.edu.cn

Abstract

Tumor spatial heterogeneity analysis requires precise correlation between Hematoxylin and Eosin (H&E) morphology and immunohistochemical (IHC) biomarker expression, yet current methods suffer from spatial misalignment in consecutive sections, severely compromising in situ pathological interpretation. In order to obtain a more accurate virtual staining pattern, We propose PRINTER, a weakly-supervised framework that integrates **PR**ototype-**dr**iven content and **stai**Ning **pat**TERn decoupling and deformation-aware adversarial learning strategies designed to accurately learn IHC staining patterns while preserving H&E staining details. Our approach introduces three key innovations: (1) A prototype-driven staining pattern transfer with explicit content-style decoupling; and (2) A cyclic registration-synthesis framework GapBridge that bridges H&E and IHC domains through deformable structural alignment, where registered features guide cross-modal style transfer while synthesized outputs iteratively refine the registration; (3) Deformation-Aware Adversarial Learning: We propose a training framework where a generator and deformation-aware registration network jointly adversarially optimize a style-focused discriminator. Extensive experiments demonstrate that PRINTER effectively achieves superior performance in preserving H&E staining details and virtual staining fidelity, outperforming state-of-the-art methods. Our work provides a robust and scalable solution for virtual staining, advancing the field of computational pathology.

CCS Concepts

• Applied computing → Life and medical sciences.

*Both authors contributed equally to this research.

†Corresponding author.

Permission to make digital or hard copies of all or part of this work for personal or classroom use is granted without fee provided that copies are not made or distributed for profit or commercial advantage and that copies bear this notice and the full citation on the first page. Copyrights for components of this work owned by others than the author(s) must be honored. Abstracting with credit is permitted. To copy otherwise, or republish, to post on servers or to redistribute to lists, requires prior specific permission and/or a fee. Request permission from permissions@acm.org.
MM '25, Dublin, Ireland.

© 2025 Copyright held by the owner/author(s). Publication rights licensed to ACM.
ACM ISBN 979-8-4007-2035-2/2025/10
<https://doi.org/10.1145/3746027.3755487>

Keywords

Virtual Staining, Weakly-Supervised, Prototype-Driven, Deformation-Aware Adversarial Learning, Computational Pathology

ACM Reference Format:

Yizhe Yuan, Bingsen Xue, Bangzheng Pu, Chengxiang Wang, and Cheng Jin. 2025. PRINTER: Deformation-Aware Adversarial Learning for Virtual IHC Staining with In Situ Fidelity. In *Proceedings of the 33rd ACM International Conference on Multimedia (MM '25)*, October 27–31, 2025, Dublin, Ireland. ACM, New York, NY, USA, 10 pages. <https://doi.org/10.1145/3746027.3755487>

1 Introduction

Understanding the spatial heterogeneity of tumors and its association with disease initiation and progression is a cornerstone of cancer biology. Current histopathological workflows heavily rely on Hematoxylin and Eosin (H&E) staining and immunostaining of serial sections through immunohistochemistry (IHC) staining [31]. However, this process is cumbersome, tissue-exhaustive, and prone to misalignment of tissue images. Additionally, compared to H&E staining, IHC staining involves a more complex and expensive preparation process, limiting its widespread application in clinical practice [23]. Therefore, translating H&E to IHC staining could serve as an ideal solution for obtaining IHC-stained images.

Recent advances in GANs have significantly enhanced virtual staining [26, 30, 47]. However, current methods are typically constrained to either fully unpaired training (with [31] or without [39] manual annotations) or strictly [6] aligned paired data. Since it is often hard to acquire strictly aligned paired data, recent work has proposed methods using loosely [3, 21, 45] aligned pairs to extract optimal supervision, providing a more adaptable and practical solution. However, existing methods either tolerate misalignment or extract supervised signals from neighboring slices, but challenges of structural inconsistencies still remain, including preserving the staining details of the original H&E images and learning the correct IHC staining.

The difficulty of IHC virtual staining from serial H&E sections lies in the following aspects: 1) *The specificity of IHC staining.* IHC staining is designed to detect the expression of specific target proteins (e.g., CD3, PAX5, ER, HER2), for specific cells or tissue regions, while H&E staining provides comprehensive histomorphological information. 2) *Structural inconsistencies caused by serial sectioning.* Although serial sections from the same specimen typically have

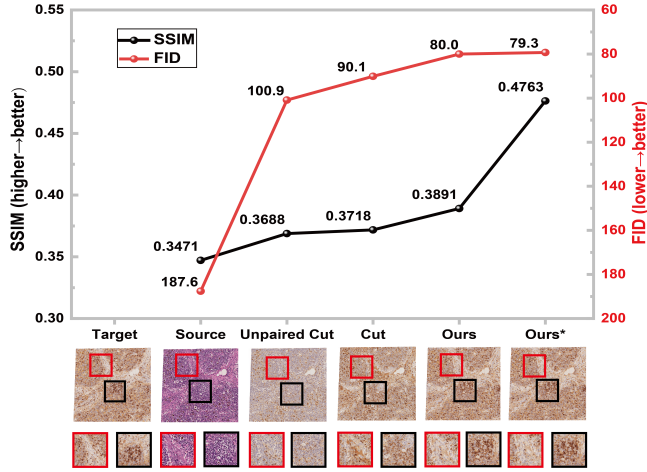


Figure 1: Structural Misalignment Hinders Domain Adaptation: An SSIM and FID Analysis. From left to right: original H&E and IHC; image generated by unpaired training setup CUT; image generated by paired training setup CUT; image generated by our method; and the image after applying the deformation.

a thickness of only 2–5 μm , minor spatial displacements and morphological variations between adjacent sections may still occur during sections preparation. 3) *Conflict between content preservation and staining pattern learning.* The virtual staining model must maximally preserve the original tissue morphology and detailed information from HE images. This requires the model to capture the key signal characteristics of IHC during cross-domain mapping without neglecting the holistic structural information provided by H&E staining.

The essence of virtual staining is image transformation. To tackle structural inconsistency, besides accepting pixel-level differences between adjacent slices or using unpaired training, another approach is to reduce these inconsistencies with image alignment techniques [23]. One common strategy aligns the generated image—after it passes through the discriminator—with the target using L1/L2 loss [11]. While this improves spatial alignment, it often fails to preserve fine-grained staining details and leads to discrepancies in data distribution [4, 32]. In fact, there is an essential problem, which is that structural inconsistency can lead to differences in data distribution [13, 44]. In addition, keeping the generated modality content-consistent with the original modality [16, 30, 31], can lead to conflicts in the learning of the staining patterns. A better strategy is to decouple the content and the staining pattern, typically employing learnable encodings to drive staining modality learning [9, 42]. However, the intricacy of staining patterns poses a significant challenge in designing a semantically rich staining framework to guide staining synthesis.

To address these challenges, we developed a novel weakly supervised intensity and structure unbiased style transfer model, named PRINTER, for high-quality H&E to IHC virtual staining generation. Specifically, we introduced an explicit content-style decoupling

method based on learnable prototypes, which successfully resolved the fundamental conflict between content preservation and style migration in cross-modal virtual coloring by decomposing IHC coloring patterns into a dictionary of migratable style prototypes. Subsequently, we established a cyclic alignment synthesis framework, GapBridge, which achieved accurate cross-domain alignment between the generated and target images by iteratively optimizing deformable alignment and virtual staining. Additionally, we aimed to eliminate the interference of structural discrepancies on the discriminator, enabling it to focus on distinguishing staining patterns. We provided a structurally distorted throw pressure to the generator through the alignment network, jointly deceiving the discriminator. Meanwhile, the discriminator was designed to refine coloring details as closely as possible to accurately distinguish structurally consistent images. Fig. 1 illustrated the learning gain in staining patterns from unpaired to paired training CUT [30], as well as the gradual reduction of structural inconsistency using our method.

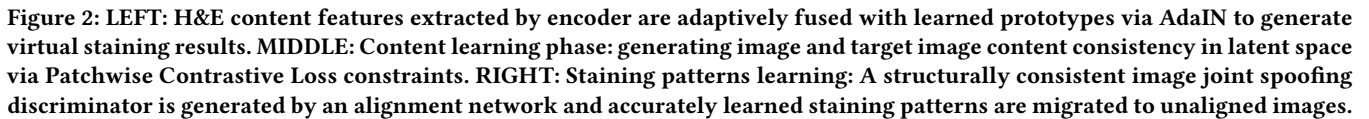
The primary contributions of this work are three-fold:

- (1) **Prototype-Driven Virtual Staining:** We propose a novel prototype-driven framework for precise virtual staining from H&E to IHC images, which effectively resolves the fundamental conflict between content preservation and staining pattern learning.
- (2) **Dual-Network Adversarial Learning:** We introduce an innovative cooperative adversarial framework where a jointly trained generator and registration network collaboratively challenge the discriminator. This unique architecture forces the discriminator to develop more discriminative capabilities at both tissue and cellular levels, serving as a *GapBridge* that significantly enhances the quality of virtual staining generation.
- (3) **Comprehensive Experimental Validation:** Through extensive quantitative and qualitative experiments, we demonstrate the superior performance of our method in preserving H&E structural details while achieving precise stain pattern transfer. Ablation studies provide insights into virtual staining mechanisms, offering valuable perspectives for future research in computational histopathology.

2 Related Work

2.1 Image-to-image translation

Image translation techniques aim to maintain the content of the original image while mimicking the stylistic features of the target domain [17, 22, 38], which are mainly categorized into paired [41] and unpaired methods. Pix2Pix [15] pioneered pixel-level supervised transformation based on the conditional GAN [16, 20] for pixel-level supervised transformation, and Pix2PixHD [35] and InstructPix2Pix [2] respectively improve the resolution and command control capabilities, respectively. To address the data matching challenge, CycleGAN [47] adopts the cyclic consistency assumption, but this bijection assumption often does not hold in structured transformations. CUT [30] breaks through this limitation and enhances the local feature alignment through contrast learning, which demonstrates the advantage in stylized transformation [31]. Existing methods, although suitable for virtual staining from H&E to



The earliest virtual staining models operated in a paired setting using various types of GANs [24, 37]. Successful cases of paired models include translating H&E images to special stains such as PAS, PAM, and MASSON [6, 40], as well as translating H&E to IHC [25]. However, in practice, re-staining is not routinely practiced, and sequential sections are difficult to align accurately. For this reason, the unpaired staining conversion model was developed for H&E to IHC specialized staining conversion and frozen-FFPE section conversion[18, 29]. While these unpaired translation methods alleviate the need for perfect alignment, they often sacrifice staining accuracy due to a complete lack of structural guidance. The ASP method treats neighboring slices as noisy paired positive samples and tolerates pixel-level misalignment by dynamically suppressing mismatched regions through an adaptive weighting mechanism. The PPT method introduces the patch alignment method

Deformable medical image registration using deep learning has gained significant attention recently [19, 27, 34]. Traditional cross-modal image registration methods typically align raw images acquired from different modalities (e.g., CT, MRI, PET) [7, 8, 28]. However, due to substantial differences in imaging principles and feature representations across modalities, direct cross-modal registration remains highly challenging [46]. To mitigate this, recent studies have proposed cross-modal image translation methods [4, 13], which reduce inter-modality discrepancies by translating source modality images into pseudo-target modality images. Nevertheless, existing

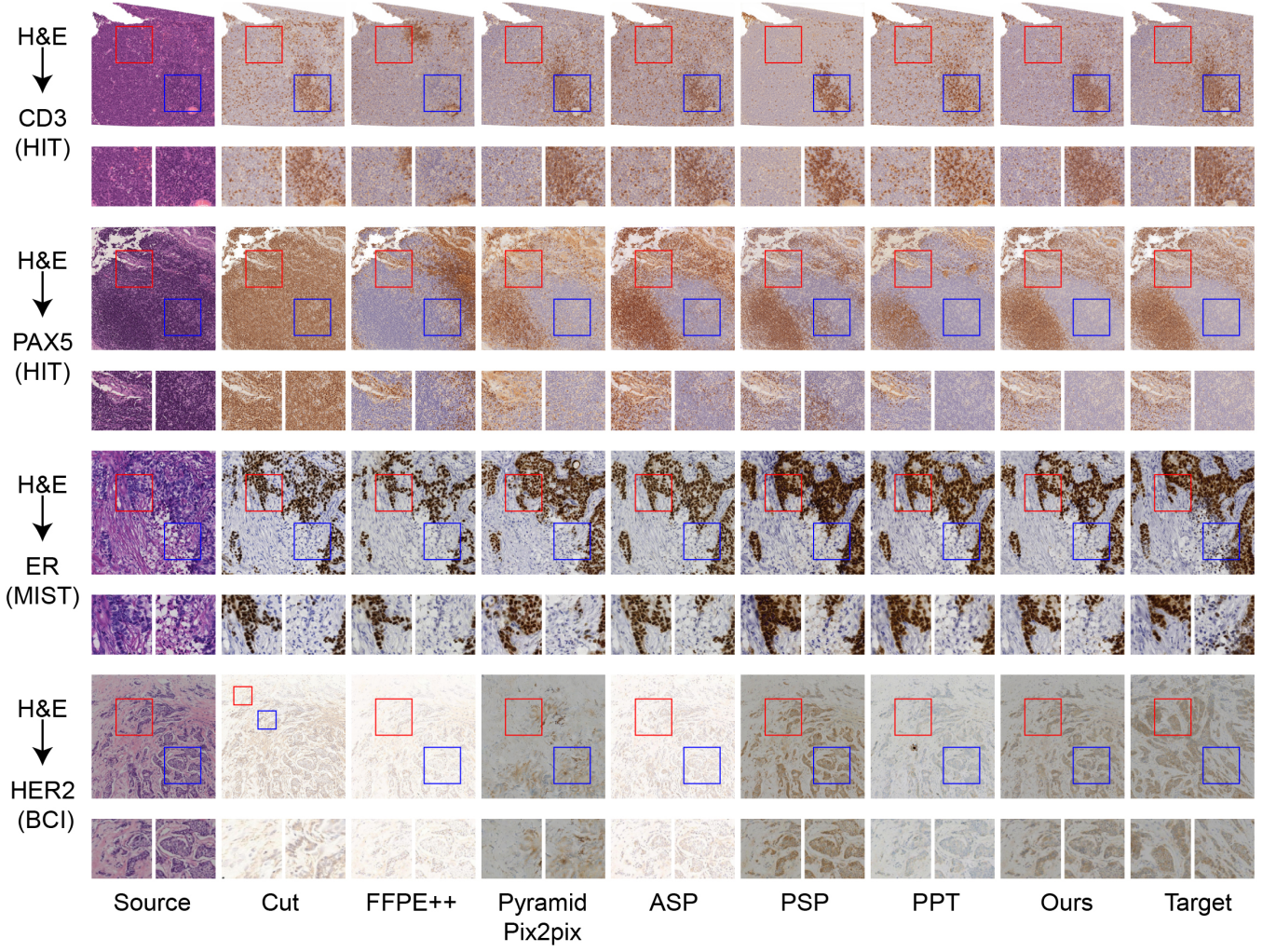


Figure 3: Qualitative comparison of virtual staining results from H&E to four immunohistochemical markers: CD3, PAX5, ER, and HER2.

works frequently overlook the potential of using registration to bridge domain gaps for better image translation.

3 Methodology

The virtual staining process can be imagined as a copy printer, which preserves tissue morphology from input sections and renders outputs by learned staining patterns. Therefore, PPrototype-driven content and stainNing patTERn decoupling and deformation-aware adversarial learning strategies (PRINTER) are proposed to resolve the inherent conflict between staining pattern fidelity and content preservation, as well as the challenges in achieving precise staining pattern transfer.

3.1 Prototype-Driven Virtual Staining

3.1.1 Style Quantization via Learnable Prototypes. Our framework extracts the content features of H&E and IHC images through the explicit content encoder, and the style encoder extracts the

staining pattern features of IHC images. While the reference image is visible during training, it is not visible during inference. Therefore, we propose a staining pattern representation based on learnable prototypes. The system maintains K trainable prototypes $\mathcal{P} = \{\mathbf{p}_1, \dots, \mathbf{p}_K\}$ ($\mathbf{p}_k \in \mathbb{R}^8$) that discretize the continuous style space. Each input style vector \mathbf{s} is quantized through Sinkhorn optimal transport [5].

$$\mathbf{s}_q = \sum_{k=1}^K \alpha_k \mathbf{p}_k, \quad \alpha_k = \text{Sinkhorn}(\mathbf{s}, \mathcal{P}, \tau = 0.1) \quad (1)$$

where the temperature τ controls assignment sharpness. This soft-quantization approach maintains end-to-end micronutrability while ensuring that all prototypes are utilized in a balanced manner. Notably, these prototypes are not static, but evolve with the training process. Each prototype is updated with momentum based on the

Table 1: Evaluation Metrics for Different Datasets and Methods

Dataset	Method	Content Consistency		Staining pattern Consistency				Avg. Rank ↓
		SSIM↑	PSNR↑	SSIM↑	PSNR↑	LPIPS↓	FID↓	
H&E → CD3 (HIT)	CUT [30]	0.7600	17.4210	0.3718	17.8735	0.2815	90.0959	3.3
	FFPE++ [18]	0.6810	16.3589	0.3728	17.4980	0.3040	95.1369	5.3
	PyramidPix2Pix [25]	0.3535	14.6172	0.3699	18.2900	0.2814	101.6701	5.2
	ASP [21]	0.7180	16.9185	0.3655	17.5943	0.2846	87.7009	4.7
	PSP [3]	0.7297	15.3891	0.3769	17.7803	0.2675	85.3342	3.2
	PPT [45]	0.6501	16.4615	0.3694	17.4713	0.2913	86.1170	5.3
	Ours	0.7926	17.8303	0.3891	18.5368	0.2501	80.0493	1.0
H&E → PAX5 (HIT)	CUT [30]	0.6239	15.6086	0.3136	16.5285	0.3372	94.4340	5.2
	FFPE++ [18]	0.6360	15.2646	0.3133	16.5407	0.3412	98.4873	5.8
	PyramidPix2Pix [25]	0.2906	13.7026	0.3063	17.1182	0.3140	94.5621	6.2
	ASP [21]	0.6778	16.0870	0.3164	17.1589	0.3041	85.1021	3.2
	PSP [3]	0.7008	14.4579	0.3320	17.4880	0.2892	85.1455	2.5
	PPT [45]	0.6098	15.5375	0.3215	17.4177	0.3006	84.6294	3.2
	Ours	0.7161	16.1967	0.3146	17.2136	0.2936	81.4670	2.0
H&E → ER (MIST)	CUT [30]	0.7022	13.9971	0.1781	13.5509	0.4551	38.9496	4.3
	FFPE++ [18]	0.7133	13.6216	0.1822	13.7272	0.4645	38.7274	4.2
	PyramidPix2Pix [25]	0.1282	11.2563	0.1768	14.8679	0.4484	70.6640	5.5
	ASP [21]	0.7304	13.6786	0.1773	14.3131	0.4332	33.6365	3.0
	PSP [3]	0.6742	12.8929	0.1573	14.3406	0.4307	35.9693	4.7
	PPT [45]	0.6337	13.5170	0.1828	14.6017	0.4166	33.9854	3.0
	Ours	0.6708	13.3091	0.1675	14.9855	0.4287	32.0808	3.3
H&E → HER2 (BCI)	CUT [30]	0.7074	9.9543	0.3694	14.7774	0.4587	51.1016	4.3
	FFPE++ [18]	0.6872	9.5321	0.4082	14.7326	0.4507	54.1656	4.8
	PyramidPix2Pix [25]	0.2878	16.5655	0.3593	16.6875	0.4962	125.8636	5.7
	ASP [21]	0.7035	9.8983	0.3663	14.9383	0.4420	68.0847	4.8
	PSP [3]	0.6640	14.6418	0.3951	19.5338	0.4269	38.7137	2.7
	PPT [45]	0.6709	11.7057	0.3646	16.8532	0.4250	62.3313	4.0
	Ours	0.7315	18.1639	0.4368	19.1816	0.4271	42.1208	1.7

Table 2: Content Consistency Evaluation (X vs \hat{Y})

Method	SSIM↑	PSNR↑
Baseline	0.6501	16.4615
Reg-only	0.6606	16.3403
No-Adversarial	0.7519	17.0020
No-NMI	0.7618	17.2791
Learnable Vector	0.7548	17.5876
Direct Encoding	0.7597	17.0488
Gen-Registration	0.7956	17.4777
Ours	0.7926	17.8303

mean value of its corresponding staining pattern feature:

$$\mathbf{p}_k^{(t+1)} \leftarrow \text{Norm}(0.9\mathbf{p}_k^{(t)} + 0.1\bar{\mathbf{s}}_k) \quad (2)$$

where $\bar{\mathbf{s}}_k$ is the mean of features assigned to prototype k , and $\text{Norm}(\cdot)$ enforces unit sphere projection.

3.1.2 Prototype-Conditioned Image Generation. The quantized style \mathbf{s}_q drives the staining process through:

$$\hat{\mathbf{y}} = D(\mathbf{f}_c, \mathbf{s}_q), \quad \mathbf{s}_q = g_\theta(\mathbf{f}_c, \mathcal{P}) \quad (3)$$

where g_θ is the prototype aggregator that predicts assignment weights from content features \mathbf{f}_c . The decoder D employs AdaIN [14] layers to achieve a characteristic blend of content and style:

$$\text{AdaIN}(\mathbf{f}_c, \mathbf{s}_q) = \gamma \mathbf{s}_q \odot \frac{\mathbf{f}_c - \mu}{\sigma} + \beta \mathbf{s}_q \quad (4)$$

3.2 GapBridge: Deformation-Aware Cross-Modal Registration

To address cross-modal misalignment, we propose a dual-path alignment framework that integrates deformation-based registration with content-aware contrastive learning. The framework employs a VoxelMorph network R [1] to predict a deformation field $\phi = R(X, Y)$, which warps the synthesized image \hat{Y} to align with the target Y through the transformation $\hat{Y} = W_\phi(\hat{Y})$. While this registration step helps correct structural mismatches, we further enhance content consistency between \hat{Y} and the target H&E images by incorporating a patch-wise contrastive loss \mathcal{L}_{cont} , inspired by CUT

Table 3: Generated Image Quality Evaluation (Y vs \hat{Y})

Method	SSIM \uparrow	PSNR \uparrow	LPIPS \downarrow	FID \downarrow
Baseline	0.3694	17.4713	0.2913	86.1170
Reg-only	0.3654	17.5546	0.2755	80.1318
No-Adversarial	0.3687	17.7544	0.2806	85.3821
No-NMI	0.3665	17.5540	0.2707	82.4281
Learnable Vector	0.3966	18.7112	0.3196	139.5715
Direct Encoding	0.3647	17.9268	0.2564	74.1877
Gen-Registration	0.3845	18.3411	0.2603	82.7541
Ours	0.3891	18.5368	0.2501	80.0493

[30]. This content-aware contrastive learning mechanism reduces the burden on the generator by explicitly maintaining semantic correspondence between corresponding regions, complementing the geometric alignment achieved through deformation. The combined approach ensures both structural and semantic alignment across modalities.

This joint approach simultaneously addresses three critical challenges in cross-modal image translation:

- **Geometric misalignment:** Differentiable registration corrects structural distortions through ϕ -based warping
- **Semantic inconsistency:** Contrastive learning maintains content fidelity via \mathcal{L}_{cont}
- **Bidirectional registration-migration synergy:** Forward (stain migration \rightarrow cross-modal interference removal) and backward (registration \rightarrow structural consistency \rightarrow accurate stain transfer)

3.2.1 Multi-Scale Structural Alignment. We propose a hierarchical alignment framework combining three complementary losses to ensure both local and global consistency:

$$\mathcal{L}_{align} = \underbrace{\|\tilde{Y} - Y\|_1}_{\text{pixel-level}} + \underbrace{\sum_l \|\Phi_l(\tilde{Y}) - \Phi_l(Y)\|_1}_{\text{perceptual}} + \underbrace{\sum_s \|P_s(\tilde{Y}) - P_s(Y)\|_1}_{\text{multi-scale}} \quad (5)$$

where Φ_l denotes the l -th layer activation of a pretrained VGG network [31], and P_s represents Gaussian pyramid decomposition at scale s [25]. This unified formulation simultaneously enforces fine-grained intensity matching through L1 loss, maintains high-level semantic consistency via VGG perceptual loss, and preserves structural coherence across spatial scales using pyramid loss.

3.2.2 Transitional deformation suppression. While adjacent histological slices share similar anatomical structures, significant variations may still exist due to cutting artifacts, staining differences, or biological variability. Traditional registration methods that enforce strict pixel-level alignment can distort important tissue morphology. Our structure-preserving registration framework addresses this challenge through:

$$\mathcal{L}_{reg} = \underbrace{-\log(\gamma - \text{NMI}(\tilde{Y}, Y))}_{\text{adaptive similarity}} + \underbrace{\lambda \mathcal{R}(\phi)}_{\text{deformation control}} \quad (6)$$

By using NMI [10] to constrain the similarity between the deformed source image and the target image, along with a smoothness loss [4] to suppress excessive deformation fields, the problem of image distortion and warping can be effectively mitigated.

3.2.3 Total Registration Objective. The final objective function for the registration module integrates all constraints:

$$\mathcal{L}_{total} = \lambda_{cont} \mathcal{L}_{cont} + \lambda_{align} \mathcal{L}_{align} + \lambda_{reg} \mathcal{L}_{reg} \quad (7)$$

where λ_{cont} , λ_{align} and λ_{reg} control the relative importance of each term. All default to 1 in our experiments.

3.3 Adversarial Training for Distribution Rendering

In traditional adversarial training, it is commonly assumed that the discriminator's role is to determine whether the generated data is real. However, the criteria for this judgment are not explicitly defined. When faced with two unpaired images, should the discriminator focus on assessing structural authenticity or staining pattern authenticity? Based on this observation, we propose that the registration network R assists the generator G in mitigating interference caused by structural misalignment. Simultaneously, this allows the discriminator to concentrate solely on evaluating staining patterns, thereby forming an implicit registration supervision signal. The adversarial objective consists of:

$$L_{adv} = \min_{G,R} \max_D \left(\mathbb{E}_{Y \sim p_{data}} [\log D(Y)] + \mathbb{E}_{X \sim p_{source}} [\log (1 - D(R(G(X))))] \right) \quad (8)$$

where the expectations are taken over real and generated distributions respectively.

The registration supervision emerges through:

$$\nabla_{\theta_R} L_{adv} = \mathbb{E}_{\tilde{Y} \sim p_G} \left[\frac{\partial L_{adv}}{\partial \tilde{Y}} \cdot \frac{\partial \tilde{Y}}{\partial R} \cdot \frac{\partial R}{\partial \theta_R} \right] \quad (9)$$

where θ_R represents the registration network parameters, and R denotes the registration transformation. This supervision signal is self-driven, meaning the registration network can learn without any ground truth displacement annotations, instead improving through the generator's failures. When the discriminator rejects a synthetic image with structural misalignment, the registration network must collaborate with the generator to produce structurally consistent and realistic staining results. This adversarial cooperation establishes a dynamic game-theoretic framework for geometric reasoning.

4 Experiments

4.1 Settings

Dataset. Since our task is to achieve virtual staining from H&E to IHC using adjacent tissue slices, we have collected the following datasets:

- (1) **HIT dataset** [45]: It includes 652 image pairs for training and 155 image pairs for testing in the H&E-CD3 (T-cell marker) dataset, as well as 1614 image pairs for training and 163 image pairs for testing in the H&E-PAX5 (B-cell marker) dataset.

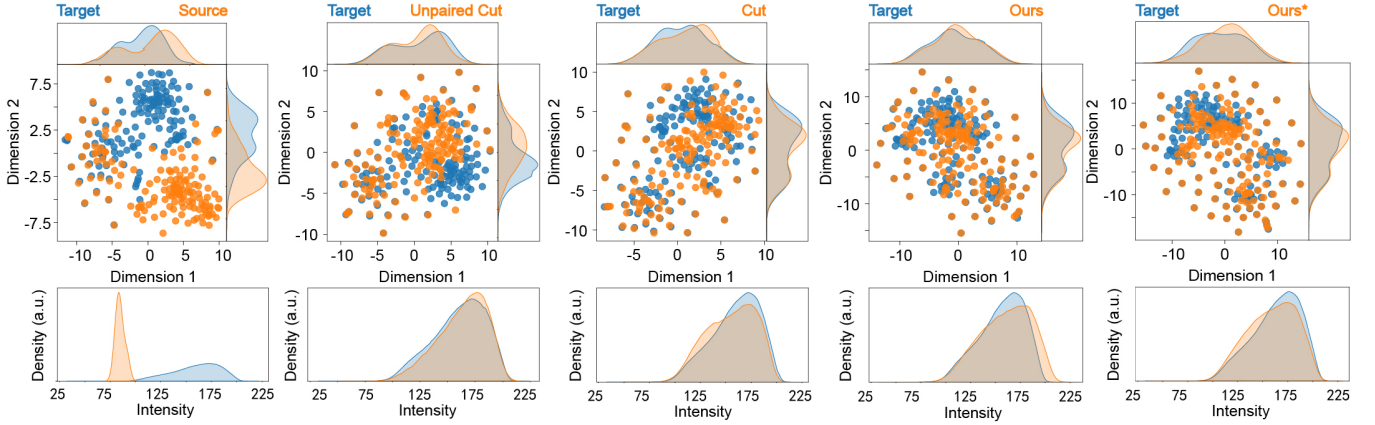


Figure 4: Illustration of the domain offset problem using T-SNE visualization. The yellow and blue dots indicate two images with different domains. From left to right: original H&E and IHC; image generated by unpaired training setup CUT; image generated by paired training setup CUT; image generated by our method; image after applying the distortion and IHC. the second row shows the distribution of positive cells in the source (generated domain) and target domain samples using color space contrast statistics.

Table 4: Registration Quality Evaluation (\tilde{Y} vs Y)

Method	SSIM \uparrow	PSNR \uparrow	LPIPS \downarrow	FID \downarrow
Baseline	-	-	-	-
Reg-only	0.4024	18.2429	0.2592	79.8989
No-Adversarial	0.4469	19.1235	0.2741	89.3116
No-NMI	0.4083	18.3435	0.2572	80.9087
Learnable Vector	0.4441	19.3734	0.3180	140.1121
Direct Encoding	0.4118	18.7166	0.2367	73.2241
Gen-Registration	0.4877	19.8522	0.2259	82.2434
Ours	0.4763	19.8431	0.2315	79.2665

- (2) **BCI dataset** [25]: Collected from breast cancer tissues with a resolution of 1024×1024 , it consists of 3896 H&E-HER2 pairs for training and 977 pairs for testing.
- (3) **ER dataset from the MIST dataset** [21]: It includes 4153 pairs for training and 1000 pairs for testing, with a resolution of 1024×1024 .

Baseline. We selected six state-of-the-art baseline methods for a comprehensive comparison, including methods that leverage approximately paired data to tolerate structural inconsistencies, such as FFPE++ [18], and CUT [30], as well as unpaired methods like PyramidPix2Pix [25], ASP [21], PSP [3], and PPT [45].

Implementation details. We adopt the baseline model provided by the PPT [45] framework for training. All images are uniformly resized to 512×512 , and the model is trained for 200 epochs. All experiments are conducted on an NVIDIA RTX 4090 GPU. For detailed hyperparameter configurations, please refer to our GitHub repository.

Evaluation metrics. We employ Peak Signal-to-Noise Ratio (PSNR) and Structural Similarity Index Measure (SSIM) to quantify pixel-level similarity between images [36]. To further assess the quality of generated images, we utilize Fréchet Inception Distance

(FID) [12] to measure the feature-level distance between image distributions and Learned Perceptual Image Patch Similarity (LPIPS) [43] to evaluate perceptual similarity as perceived by the human visual system. Additionally, we comprehensively analyze the performance of our method by comparing the SSIM and PSNR between the generated images and the original images, as well as the SSIM, PSNR, FID, and LPIPS between the deformed images generated by our method and the target images.

4.2 Main Results

Qualitative comparison. Figure 3 compares the virtual staining performance of our method versus six state-of-the-art methods on four biomarker targets: CD3, PAX5, ER, and HER2. Our method achieves a good trade-off between content preservation and style consistency. Previous methods either overly prioritize content consistency at the expense of realistic staining patterns or excessively align with the target image, leading to distortions in tissue structure. For example, while CUT [30] and FFPE++ [18] methods utilize contrastive loss to enforce content consistency and learn distribution consistency through discriminators, the lack of an accurate staining model transfer mechanism results in insufficient precision in staining details, particularly in the staining intensity and morphological features of positive cells, which deviate significantly from real staining. The PyramidPix2Pix [25] introduces a pixel-level tolerance mechanism, relaxing the strict constraints on structural consistency, thereby generating relatively accurate staining patterns. However, this method underperforms in preserving H&E image details, leading to the loss of some tissue structures and cellular morphological details, which compromises the completeness and practicality of the staining results. Additionally, ASP [21], PSP [3], and PPT [45] methods attempt to optimize the learning of staining patterns by leveraging the best information provided by adjacent slices while preserving H&E details. However, these methods heavily rely on data quality, resulting in limited generalization

ability and difficulty in adapting to diverse staining scenarios. In contrast, our method accurately preserves H&E staining details while presenting precise staining patterns.

Quantitative results. We quantitatively compared the performance of our proposed method with other SOTA methods on the HIT [45], MIST [21], and BCI [25] datasets. All compared methods were implemented strictly following the conditions in their original papers or using their open-source code, with the results presented in Table I 1. The experiments demonstrate that our method achieves the best performance in terms of content consistency (e.g., SSIM, PSNR) between the generated and original images, as well as staining pattern consistency (e.g., FID) between the generated and target images, fully validating the effectiveness of our virtual staining approach.

Specifically, unpaired methods such as CUT [30] and FFPE++ [18] performed better in terms of content consistency, but the staining pattern consistency was poor due to insufficient supervised signals from neighboring IHC slices. The fully supervised method PyramidPix2Pix [25] improves staining through pixel-level optimization, but FID performance is limited by forced alignment of weakly paired images. This problem is particularly prominent in BCI [25] datasets containing severely misaligned samples. ASP [21] and PPT [45], although considering weakly paired features, directly align the generated and target images, ignoring the effect of tissue deformation. PSP [3] improves performance with the help of pre-trained segmentation networks, but increases computational complexity.

Our model demonstrates superior performance advantages across multiple key metrics. Specifically, in terms of content retention performance, the model achieves state-of-the-art results on all datasets except ER protein staining. In terms of FID metrics, our method performs optimally for CD3 (FID=80.0493), PAX5 (FID=81.4670), and ER (fid=32.0808) markers, and only slightly underperforms the PSP [3] model, which requires an additional cell segmentation step, on the HER2 staining. It is particularly noteworthy that on the CD3 protein, our method achieved the best performance on all evaluation metrics: the FID metric was improved by 6.19% compared to the suboptimal PSP [3] model; and the SSIM and PSNR were significantly improved by 21.9% and 8.32%, respectively, compared to the baseline method PPT [45].

4.3 Ablation Study

Our ablation experiments systematically evaluate the contributions of each key component in the model, specifically designing the following six comparison schemes: (1) Reg-only: remove the style decoupling mechanism of the prototype bootstrap and retain only the alignment module; (2) No-Adversarial: the alignment images are not involved in adversarial training; (3) No-NMI: remove the NMI loss used to constrain the deformation field; (4) Learned Vector: adopting learnable style vectors instead of the decoupling strategy of the prototype library; (5) Direct Encoding: assuming that the target image encoding can be directly obtained at the inference stage; (6) Gen-Registration: inputting the generated images into the deformation network instead of the original H&E images.

The experimental results show that in terms of content retention, all the improved methods can better preserve H&E image details,

with the Gen-Registration method performing closest to the final model, indicating that the participation of the generated image in deformation alignment can effectively enhance the transmission of content information. In terms of coloring pattern consistency, although the Reg-only method performs better in FID metrics, its SSIM and PSNR metrics are poorer due to the lack of an effective decoupling mechanism, which highlights the importance of decoupling the content from the coloring pattern; at the same time, it is difficult to accurately capture the target coloring features in the learnable style vectors, which further verifies the advantage of the prototype-guided strategy. In addition, the alignment network outperforms the unaligned scheme in all evaluation metrics, which confirms that the module not only realizes structural alignment, but also improves the fitting effect of the coloring pattern by reducing the inter-domain differences, and plays a key role as a bridge in the cross-domain transformation. Moreover, if the reference image is available at the time of inference, the in situ staining effect of virtual staining can be further enhanced.

4.4 Further analysis

The experimental results show that the indexes of the aligned images match more closely with the neighboring tissue slices, a finding that is consistent with the results presented in Figure 1. To elucidate the principle of the method, we visualized the images generated by different training strategies using the t-SNE technique [33] in Fig. 4, combined with a statistical comparison of the distribution of the number of positive cells in the color space. The visualization results reveal two key phenomena: first, there is a significant difference between the initial data distribution in the source domain (yellow) and the target domain (blue); second, the distributions in the t-SNE space gradually converge to be close to each other with the improvement of the structural similarity between the input image and the reference image (SSIM) as well as the optimization of the training strategy. This result quantitatively verifies the effectiveness of the alignment network proposed in this study in reducing the inter-domain differences, thus providing strong support for the accurate learning of staining patterns.

5 Conclusion

Our method demonstrates significant improvements in virtual staining by addressing two critical aspects: preserving detailed information from the original slices and accurately learning the staining patterns. By introducing a deformation network, we effectively reduce structural inconsistencies and minimize the domain gap, leading to enhanced structural alignment and reduced metrics such as LPIPS and FID. The dynamic registration mechanism, driven by adversarial learning, further optimizes the alignment between source and target domains, resulting in more realistic and visually coherent generated images. Additionally, our approach exhibits strong scalability, extending beyond virtual staining to other image transformation tasks with approximate pairing and achieving robust registration capabilities. These advancements underscore the effectiveness and versatility of our method in handling complex image translation challenges.

Acknowledgements

This work was supported by the National Key R&D Program of China (No. 2022YFB4702702).

References

- [1] Guha Balakrishnan, Amy Zhao, Mert R Sabuncu, John Guttag, and Adrian V Dalca. 2019. Voxelmorph: a learning framework for deformable medical image registration. *IEEE transactions on medical imaging* 38, 8 (2019), 1788–1800.
- [2] Tim Brooks, Aleksander Holynski, and Alexei A Efros. 2023. Instructpix2pix: Learning to follow image editing instructions. In *Proceedings of the IEEE/CVF conference on computer vision and pattern recognition*. 18392–18402.
- [3] Fuqiang Chen, Ranran Zhang, Boyun Zheng, Yiwen Sun, Jiahui He, and Wenjian Qin. 2024. Pathological semantics-preserving learning for H&E-to-IHC virtual staining. In *International Conference on Medical Image Computing and Computer-Assisted Intervention*. Springer, 384–394.
- [4] Zekang Chen, Jia Wei, and Rui Li. 2022. Unsupervised multi-modal medical image registration via discriminator-free image-to-image translation. *arXiv preprint arXiv:2204.13656* (2022).
- [5] Marco Cuturi. 2013. Sinkhorn distances: Lightspeed computation of optimal transport. *Advances in neural information processing systems* 26 (2013).
- [6] Kevin de Haan, Yijie Zhang, Jonathan E Zuckerman, Tairan Liu, Anthony E Sisk, Miguel FP Diaz, Kuang-Yu Jen, Alexander Nobori, Sofia Liou, Sarah Zhang, et al. 2021. Deep learning-based transformation of H&E stained tissues into special stains. *Nature communications* 12, 1 (2021), 4884.
- [7] Qihua Dong, Hao Du, Ying Song, Yan Xu, and Jing Liao. 2023. Preserving tumor volumes for unsupervised medical image registration. In *Proceedings of the IEEE/CVF International Conference on Computer Vision*. 21208–21218.
- [8] Morteza Ghahremani, Mohammad Khateri, Bailiang Jian, Benedikt Wiestler, Ehsan Adeli, and Christian Wachinger. 2024. H-vit: A hierarchical vision transformer for deformable image registration. In *Proceedings of the IEEE/CVF Conference on Computer Vision and Pattern Recognition*. 11513–11523.
- [9] Xianchao Guan, Yifeng Wang, Yiyang Lin, Xi Li, and Yongbing Zhang. 2024. Unsupervised multi-domain progressive stain transfer guided by style encoding dictionary. *IEEE Transactions on Image Processing* 33 (2024), 767–779.
- [10] Mengjie Guo. 2024. Unsupervised Multi-modal Medical Image Registration via Invertible Translation. In *European Conference on Computer Vision*. Springer, 22–38.
- [11] Kaiming He, Xinlei Chen, Saining Xie, Yanghao Li, Piotr Dollár, and Ross Girshick. 2022. Masked autoencoders are scalable vision learners. In *Proceedings of the IEEE/CVF conference on computer vision and pattern recognition*. 16000–16009.
- [12] Martin Heusel, Hubert Ramsauer, Thomas Unterthiner, Bernhard Nessler, and Sepp Hochreiter. 2017. Gans trained by a two time-scale update rule converge to a local nash equilibrium. *Advances in neural information processing systems* 30 (2017).
- [13] Joel Honkamaa, Umair Khan, Sonja Koivukoski, Mira Valkonen, Leena Latonen, Pekka Ruusuvaari, and Pekka Marttinen. 2023. Deformation equivariant cross-modality image synthesis with paired non-aligned training data. *Medical Image Analysis* 90 (2023), 102940.
- [14] Xun Huang and Serge Belongie. 2017. Arbitrary style transfer in real-time with adaptive instance normalization. In *Proceedings of the IEEE international conference on computer vision*. 1501–1510.
- [15] Phillip Isola, Jun-Yan Zhu, Tinghui Zhou, and Alexei A Efros. 2017. Image-to-image translation with conditional adversarial networks. In *Proceedings of the IEEE conference on computer vision and pattern recognition*. 1125–1134.
- [16] Yuxin Jiang, Liming Jiang, Shuai Yang, and Chen Change Loy. 2023. Scenimefy: Learning to craft anime scene via semi-supervised image-to-image translation. In *Proceedings of the IEEE/CVF International Conference on Computer Vision*. 7357–7367.
- [17] Chanyong Jung, Gihyun Kwon, and Jong Chul Ye. 2022. Exploring patch-wise semantic relation for contrastive learning in image-to-image translation tasks. In *Proceedings of the IEEE/CVF conference on computer vision and pattern recognition*. 18260–18269.
- [18] Mohamad Kassab, Muhammad Jehanzaib, Kayhan Başak, Derya Demir, G Evren Keles, and Mehmet Turan. 2024. FFPE++: Improving the quality of formalin-fixed paraffin-embedded tissue imaging via contrastive unpaired image-to-image translation. *Medical Image Analysis* 91 (2024), 102992.
- [19] Hee Guan Khor, Guochen Ning, Yihua Sun, Xu Lu, Xinran Zhang, and Hongen Liao. 2023. Anatomically constrained and attention-guided deep feature fusion for joint segmentation and deformable medical image registration. *Medical Image Analysis* 88 (2023), 102811.
- [20] Bo Li, Kaitao Xue, Bin Liu, and Yu-Kun Lai. 2023. Bbdt: Image-to-image translation with brownian bridge diffusion models. In *Proceedings of the IEEE/CVF conference on computer vision and pattern recognition*. 1952–1961.
- [21] Fangda Li, Zhiqiang Hu, Wen Chen, and Avinash Kak. 2023. Adaptive supervised patchwise loss for learning h&e-to-ihc stain translation with inconsistent groundtruth image pairs. In *International Conference on Medical Image Computing and Computer-Assisted Intervention*. Springer, 632–641.
- [22] Jiahua Li, Jiuyang Dong, Shenjin Huang, Xi Li, Junjun Jiang, Xiaopeng Fan, and Yongbing Zhang. 2024. Virtual immunohistochemistry staining for histological images assisted by weakly-supervised learning. In *Proceedings of the IEEE/CVF Conference on Computer Vision and Pattern Recognition*. 11259–11268.
- [23] Yuzhu Li, Nir Pillar, Jingxi Li, Tairan Liu, Di Wu, Songyu Sun, Guangdong Ma, Kevin de Haan, Luzhe Huang, Yijie Zhang, et al. 2024. Virtual histological staining of unlabeled autopsy tissue. *Nature Communications* 15, 1 (2024), 1684.
- [24] Kechun Liu, Beibin Li, Wenjun Wu, Caitlin May, Oliver Chang, Stevan Knezevich, Lisa Reisch, Joann Elmore, and Linda Shapiro. 2023. Vsgd-net: Virtual staining guided melanocyte detection on histopathological images. In *Proceedings of the IEEE/CVF Winter Conference on Applications of Computer Vision*. 1918–1927.
- [25] Shengjie Liu, Chuang Zhu, Feng Xu, Xinyu Jia, Zhongyue Shi, and Mulan Jin. 2022. Bci: Breast cancer immunohistochemical image generation through pyramid pix2pix. In *Proceedings of the IEEE/CVF conference on computer vision and pattern recognition*. 1815–1824.
- [26] Zhiqie Liu, Lingchao Chen, Haixia Cheng, Jianpeng Ao, Ji Xiong, Xing Liu, Yaxin Chen, Ying Mao, and Minbiao Ji. 2024. Virtual formalin-fixed and paraffin-embedded staining of fresh brain tissue via stimulated Raman CycleGAN model. *Science Advances* 10, 13 (2024), eadn3426.
- [27] Mingyuan Meng, Dagan Feng, Lei Bi, and Jinman Kim. 2024. Correlation-aware coarse-to-fine mlps for deformable medical image registration. In *Proceedings of the IEEE/CVF Conference on Computer Vision and Pattern Recognition*. 9645–9654.
- [28] Tony CW Mok, Zi Li, Yunhao Bai, Jianpeng Zhang, Wei Liu, Yan-Jie Zhou, Ke Yan, Dakai Jin, Yu Shi, Xiaoli Yin, et al. 2024. Modality-agnostic structural image representation learning for deformable multi-modality medical image registration. In *Proceedings of the IEEE/CVF Conference on Computer Vision and Pattern Recognition*. 11215–11225.
- [29] Kutsev Bengisu Ozyoruk, Sermet Can, Berkan Darbaz, Kayhan Başak, Derya Demir, Guliz Irem Gokceler, Gurdeniz Serin, Uguray Payam Hacisalihoglu, Emirhan Kurtulus, Ming Y Lu, et al. 2022. A deep-learning model for transforming the style of tissue images from cryosectioned to formalin-fixed and paraffin-embedded. *Nature Biomedical Engineering* 6, 12 (2022), 1407–1419.
- [30] Taesung Park, Alexei A Efros, Richard Zhang, and Jun-Yan Zhu. 2020. Contrastive learning for unpaired image-to-image translation. In *Computer Vision—ECCV 2020: 16th European Conference, Glasgow, UK, August 23–28, 2020, Proceedings, Part IX* 16. Springer, 319–345.
- [31] Pushpak Pati, Sofia Karkampouna, Francesco Bonollo, Eva Compérat, Martina Radić, Martin Spahn, Adriano Martinelli, Martin Wartenberg, Marianna Kruthof-de Julio, and Marianna Rapsomaniki. 2024. Accelerating histopathology workflows with generative AI-based virtually multiplexed tumour profiling. *Nature machine intelligence* 6, 9 (2024), 1077–1093.
- [32] Saksham Suri, Moustafa Meshry, Larry S Davis, and Abhinav Shrivastava. 2024. GRIT: GAN Residuals for Paired Image-to-Image Translation. In *Proceedings of the IEEE/CVF Winter Conference on Applications of Computer Vision*. 4965–4975.
- [33] Laurens Van der Maaten and Geoffrey Hinton. 2008. Visualizing data using t-SNE. *Journal of machine learning research* 9, 11 (2008).
- [34] Haiqiao Wang, Dong Ni, and Yi Wang. 2024. Recursive deformable pyramid network for unsupervised medical image registration. *IEEE Transactions on Medical Imaging* 43, 6 (2024), 2229–2240.
- [35] Ting-Chun Wang, Ming-Yu Liu, Jun-Yan Zhu, Andrew Tao, Jan Kautz, and Bryan Catanzaro. 2018. High-resolution image synthesis and semantic manipulation with conditional gans. In *Proceedings of the IEEE conference on computer vision and pattern recognition*. 8798–8807.
- [36] Zhou Wang, Alan C Bovik, Hamid R Sheikh, and Eero P Simoncelli. 2004. Image quality assessment: from error visibility to structural similarity. *IEEE transactions on image processing* 13, 4 (2004), 600–612.
- [37] Georg Wölflein, In Hwa Um, David J Harrison, and Ognjen Arandjelović. 2023. Hoechstgan: Virtual lymphocyte staining using generative adversarial networks. In *Proceedings of the IEEE/CVF Winter Conference on Applications of Computer Vision*. 4997–5007.
- [38] Sidi Wu, Yizi Chen, Samuel Mermet, Lorenz Hurni, Konrad Schindler, Nicolas Gonthier, and Loic Landrieu. 2024. Stegogan: Leveraging steganography for non-bijective image-to-image translation. In *Proceedings of the IEEE/CVF Conference on Computer Vision and Pattern Recognition*. 7922–7931.
- [39] Renao Yan, Qiming He, Yiqing Liu, Peng Ye, Lianghui Zhu, Shanshan Shi, Jizhou Gou, Yonghong He, Tian Guan, and Guangde Zhou. 2023. Unpaired virtual histological staining using prior-guided generative adversarial networks. *Computerized Medical Imaging and Graphics* 105 (2023), 102185.
- [40] Xilin Yang, Bijie Bai, Yijie Zhang, Yuzhu Li, Kevin de Haan, Tairan Liu, and Aydogan Ozcan. 2022. Virtual stain transfer in histology via cascaded deep neural networks. *ACS Photonics* 9, 9 (2022), 3134–3143.
- [41] Songsen Yu, Shiqi Wu, Yifan Lin, and Jun Liang. 2024. Unpaired Multi-scenario Sketch Synthesis via Texture Enhancement. In *Chinese Conference on Pattern Recognition and Computer Vision (PRCV)*. Springer, 181–194.

- [42] Ranran Zhang, Yankun Cao, Yujun Li, Zhi Liu, Jianye Wang, Jiahuan He, Chenyang Zhang, Xiaoyu Sui, Pengfei Zhang, Lizhen Cui, et al. 2022. MVF-Stain: multiple virtual functional stain histopathology images generation based on specific domain mapping. *Medical Image Analysis* 80 (2022), 102520.
- [43] Richard Zhang, Phillip Isola, Alexei A Efros, Eli Shechtman, and Oliver Wang. 2018. The unreasonable effectiveness of deep features as a perceptual metric. In *Proceedings of the IEEE conference on computer vision and pattern recognition*. 586–595.
- [44] Tianyang Zhang, Shaoming Zheng, Jun Cheng, Xi Jia, Joseph Bartlett, Xinxing Cheng, Zhaowen Qiu, Huazhu Fu, Jiang Liu, Aleš Leonardis, et al. 2024. Structure and Intensity Unbiased Translation for 2D Medical Image Segmentation. *IEEE Transactions on Pattern Analysis and Machine Intelligence* (2024).
- [45] Wei Zhang, Tik Ho Hui, Pui Ying Tse, Fraser Hill, Condon Lau, and Xinyue Li. 2024. High-Resolution Medical Image Translation via Patch Alignment-Based Bidirectional Contrastive Learning. In *International Conference on Medical Image Computing and Computer-Assisted Intervention*. Springer, 178–188.
- [46] Haifeng Zhao, Chi Zhang, Deyin Liu, and Lin Wu. 2025. Deformation Field Fusion for Medical Image Registration. *ACM Transactions on Multimedia Computing, Communications and Applications* (2025).
- [47] Jun-Yan Zhu, Taesung Park, Phillip Isola, and Alexei A Efros. 2017. Unpaired image-to-image translation using cycle-consistent adversarial networks. In *Proceedings of the IEEE international conference on computer vision*. 2223–2232.